

Memristors Based on Ferroelectric Cu-Deficient Copper **Indium Thiophosphate for Multilevel Storage and Neuromorphic Computing**

Mengdie Li, Yanyan He, Chengyang Wang, Weng Fu Io, Feng Guo, Wenjing Jie,* and Jianhua Hao*

It is essential to explore the interactions between intrinsic ferroelectricity and ionic activities in 2D ferroelectrics for theoretically understanding and experimentally modulating device performance. Due to the tendency of Cu⁺ migration in ferroelectric copper indium thiophosphate (CIPS) and formation of Cu conductive filaments, herein, Cu-deficient CIPS (CIPS*) is employed to investigate resistive switching (RS). Different from CIPS with controllable threshold switching and write-once read-many-times (WORM) behaviors, CIPS* shows stable non-volatile digital and analog RS behaviors by controlling the operation voltage. Owing to the formation of non-stoichiometric In_{4/3}P₂S₆ (IPS) with metallic phase at the low-resistance state, the fabricated memristors demonstrate high ON/OFF ratio up to 5×10^5 and high endurance stability (>2000 cycles), which can be utilized to implement multilevel storage. And more intriguing, amplitude-dependent and polarity-independent long-term potentiation and depression can be simulated based on the analog memristors. Artificial neural network based on CIPS* synaptic memristors can realize handwritten digit recognition with the accuracy of 91.15%. Even after considering the cycle-to-cycle and device-to-device variations of the synaptic functions, the accuracy remains as high as 90.71%. Such investigations pave the way toward highly reliable memristors base on 2D ferroelectrics with potential applications in multilevel storage and neuromorphic computing.

M. Li, Y. He, C. Wang, W. Jie College of Chemistry and Materials Science Sichuan Normal University Chengdu 610066, China E-mail: wenjing.jie@sicnu.edu.cn

W. F. Io, F. Guo, J. Hao Department of Applied Physics The Hong Kong Polytechnic University Hung Hom, Kowloon, Hong Kong 999077, China

E-mail: jh.hao@polyu.edu.hk

The ORCID identification number(s) for the author(s) of this article can be found under https://doi.org/10.1002/smll.202412314

© 2025 The Author(s). Small published by Wiley-VCH GmbH. This is an open access article under the terms of the Creative Commons Attribution-NonCommercial-NoDerivs License, which permits use and distribution in any medium, provided the original work is properly cited, the use is non-commercial and no modifications or adaptations are

DOI: 10.1002/smll.202412314

1. Introduction

2D ferroelectric remains a promising subject in physics, chemistry and materials science owing to the potential applications in the field of information storage and computing.[1-3] Exploring the interactions between intrinsic ferroelectricity and ionic activities in such 2D layers is essential for understanding of 2D ferroelectrics and modulating or enhancing device performance.[4,5] Recently, a large family of 2D van der Waals layered materials of metal thiophosphates (MTPs) has been extensively studied due to the intriguing and diverse properties of ferro- or antiferroelectric characteristics.^[6] Among them, CuInP2S6 (CIPS) has received great attention owing to the intrinsic ferroelectricity at room temperature.^[7,8] The spontaneous polarization arises from the breakdown of the center symmetry in the sulfur octahedra, giving rise to the observed room-temperature ferroelectricity.[7,9] Especially, the ferroelectricity can be maintained in the 2D limit in CIPS. A series of ferroelectric field effect transistors (FeFET)^[10,11] and ferroelectric tunnel junctions (FTJ)^[12]

based on the 2D CIPS have been studied. As schematically shown in Figure 1a, there is a sulfur framework in the crystal structure of CIPS.[13] It is reported that Cu+ ions can locate at three types, i.e., intralayer positions of central octahedral Cu1 (i) and off-centered Cu2 (ii), as well as interlayer positions of Cu3 in the van der Waals (vdW) gap (iii).[14] At a temperature below Tc (\approx 320 K for CIPS), the Cu⁺ ions locate at the off-centered sites (Cu2) upward or downward from the centers of the S octahedra, giving rise to the spontaneous polarization as well as the room-temperature ferroelectricity.^[13] Furthermore, the migration of Cu⁺ ions driven by the external electric field not only generates the room-temperature ferroelectricity in CIPS, but also contributes to the ionic conductivity.[13,15,16]

In the era of the big data, neuromorphic computing is highly desirable because it can implement brain-like computing of parallel storage and processing, self-organization and self-learning activities.^[17,18] The recent widely-studied memristor is considered to be a promising candidate in neuromorphic

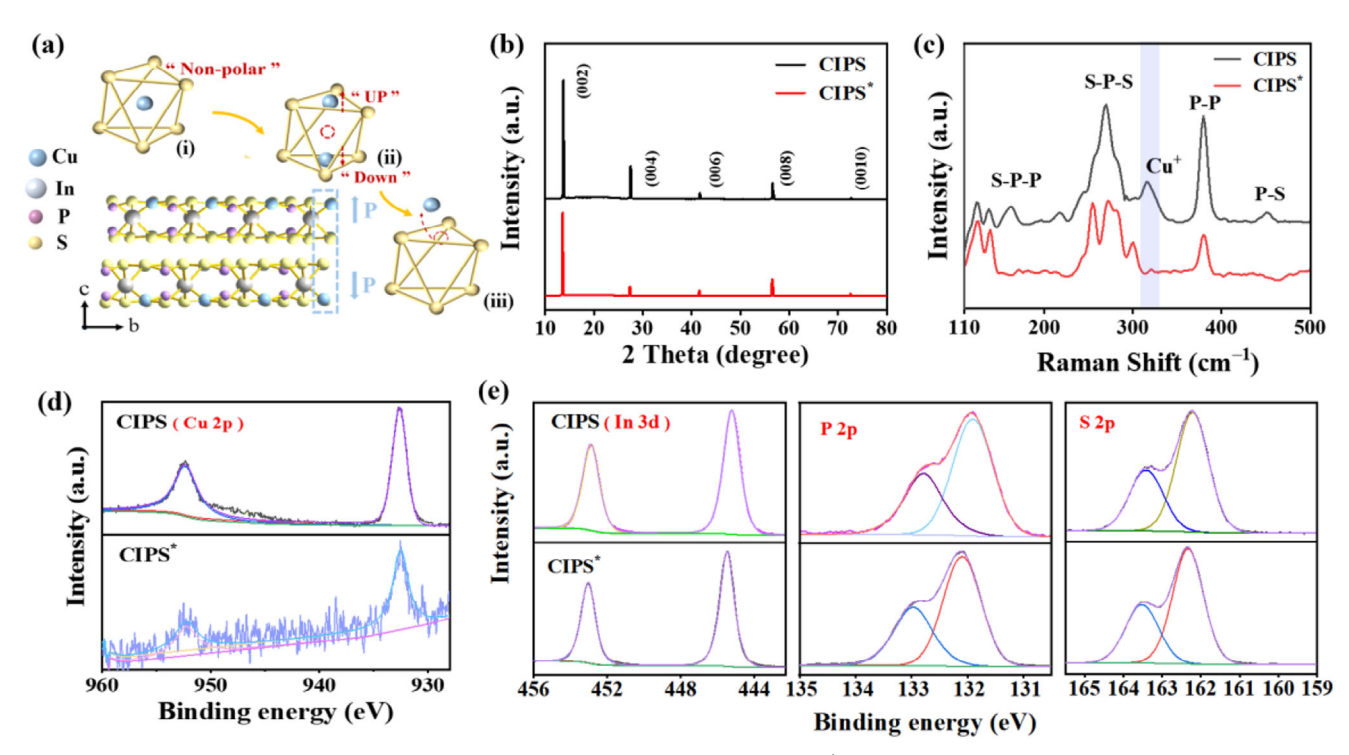


Figure 1. a) Schematic structure of the layered CIPS with illustration of the migration of Cu⁺ induced by the external electric field. b) XRD patterns of both CIPS and CIPS*. c) Raman spectra of both CIPS and CIPS*nanosheets. d) XPS spectra of Cu 2p for both CIPS and CIPS* nanosheets. e) XPS spectra of In 3d, P 2p and S 2p for both CIPS and CIPS* nanosheets.

computing.[19,20] The memristors with non-volatile properties can be utilized for artificial neurons and synaptic devices in artificial neural networks (ANNs).[21,22] Therefore, exploring potential materials with suitable RS properties and synaptic functions is also meaningful for neuromorphic computing. Recently, 2D CIPS has been studied for implementing different resistive switching (RS) behaviors and synaptic functions, [23-26] as well as successful realization of optoelectronic synapses.^[27] For example, a synaptic Au/CIPS/Ti diode was achieved based on the ferroelectric switching.^[28] Moreover, stable threshold-switching memristor based on the Cu/CIPS/graphene heterostructure was reported by utilizing the ionic conductivity under the electric field.[24] However, in CIPS, Cu⁺ ions are tend to migrate,[25] which is favorable to the formation of Cu conductive channels, inducing the direct transition from the high resistance state (HRS) to low resistance state (LRS). [13,23] However, by considering the randomness of the formed conductive filaments (CFs), the observed RS behaviors are typically not reliable. Therefore, in our experiments, Cu-deficient CIPS (CIPS*) nanosheets with low amount of Cu are employed to explore the interactions between intrinsic ferroelectricity and ionic activities, which could provide us opportunity to theoretically understand and experimentally modulate device performance. Herein, we investigate the RS properties based on Cu-deficient CIPS* nanosheets which demonstrate high-performance non-volatile bipolar RS with high ON/OFF ratio and good retention characteristics as well as high endurance stability. The high ON/OFF ratio can be utilized to achieve multilevel storage by modulating the compliance current (I_{CC}) . And more interesting, amplitude-dependent and polarityindependent long-term potentiation (LTP) and depression (LTD)

can be achieved based on the CIPS*. Such abnormal synaptic memristors could provide us opportunity to design some unique synaptic elements with diverse functionalities, and also provide a useful strategy for designing and manipulating synaptic memristors for neuromorphic computing.

2. Results and Discussion

The crystal structures of the two materials are characterized by X-ray diffraction (XRD), as shown in Figure 1b. The four distinct fingerprint peaks correspond to the (002), (004), (006) and (008), respectively, which is consistent with previously reported CIPS.^[29] All these (00*l*) diffraction peaks also can be well observed in the CIPS*, indicating the good crystalline structure of the Cudeficient materials. Then, both of the exfoliated nanosheets are analyzed using a Raman spectrometer, as shown in Figure 1c. For CIPS there is a distinct peak at 317 cm⁻¹, corresponding to the vibrational peak of Cu⁺ in the S octahedra. [30] For CIPS*, the peak at 317 cm⁻¹ is not significant due to its low Cu content. These feature peaks of CIPS* are well consistent with those of previously reported Cu-deficient CIPS.[31] Moreover, the peaks located at 240 \sim 290 cm⁻¹ are associated with S-P-S vibrations.^[32,33] The peak at 376 cm⁻¹ can be attributed to P-P stretching vibrations.^[33] When compared with CIPS, the Raman peaks of CIPS* demonstrate the lower intensity of the Cu feature peak located at 317 cm⁻¹ with the appearance of the peaks at 254 and 300 cm⁻¹, suggesting the decreased content of Cu⁺. Besides, scanning electron microscope (SEM) images show both nanosheets have uniform and smooth surfaces and the energy dispersive X-ray spectroscopy (EDS) mapping images of the elements of Cu, In, P and

CIENCE NEWS

Figure 2. a) Structure diagram of the two-terminal memristor with CIPS as the RS layer. b) Typical I-V curve of device with the TS behaviors at $I_{CC} = I$ 10^{-6} A. c) Typical I–V curves with the operation voltage of 5 V of the non-volatile bipolar and WORM RS behaviors at $I_{CC} = 10^{-4}$ A. d) Current responses to the bias voltages ranging from 6 to 10 V for a fresh Pt/CIPS*/Pt device. e) Typical I-V curve of Pt/CIPS*/Pt device with non-volatile RS behavior at I_{CC} = 10^{-5} A. f) HRS and LRS retention characteristics measured at $V_{read} = 0.5$ V for 10^4 s. g) I-V curves of the device under different I_{CC} ranging from 1 to 100 μA. h) Retention characteristics of the HRS and the five LRSs. i) Device-to-device variations of the SET and RESET voltages for 40 devices.

500

Time (s)

10⁷

10

10

10

5 nA 10 μΑ

50 nA 100 μΑ

Voltage (V)

LRS-5

1500

1000

S suggest that each element is uniformly dispersed in the two nanosheets (Figure S1, Supporting Information). Figure S2 (Supporting Information) shows the SEM-EDS spectra of the CIPS and CIPS*. The atomic percentages of the Cu, In, P and S in CIPS and CIPS* can be concluded, respectively. The content of Cu in CIPS is five times that of CIPS*. According to the elemental stoichiometry, the molecular formula of CIPS* can be expressed as Cu_{0,2}InP₂S₆. Furthermore, the elemental composition of the two materials has been analyzed by X-ray photoelectron spectroscopy (XPS), as shown in Figure 1d,e. It should be mentioned that the intensity of binding energy of Cu 2p in CIPS* is much weaker than that in CIPS, indicating the Cu deficiency in CIPS*.[34,35] While, the XPS spectra of In 3d, P 2p and S 2p show negligible differences between CIPS and CIPS*. In addition, the surface morphology and layer thickness of the exfoliated nanosheets are characterized by atomic force microscopy (AFM), as shown in Figure S3 (Supporting Information). The CIPS and CIPS* nanosheets can be confirmed with the thickness of ~ 30 nm.

To compare the different RS behaviors between CIPS and Cudeficient CIPS*, the RS properties of CIPS are studied in this work. Figure 2a schematically shows the two-terminal device with the sandwich structure of Pt/CIPS/Pt, where the CIPS nanosheet is employed to serve as the RS layer, and metal Pt is used as the bottom and top electrodes. Figure S4 (Supporting Information) demonstrates butterfly-shape hysteretic current-voltage (I-V) curves of a pristine CIPS memristor, which is generated from the intrinsic ferroelectric properties of CIPS.[13] When the operation voltage is further increased to 5 V, the device demonstrates typical volatile threshold switching behavior (TS) behavior when the I_{CC} is set to 10^{-6} A, as shown in Figure 2b. For the positive voltage scanning, the device is switched from the HRS to LRS at a threshold voltage (V_{th}) of ~ 1.0 V in the forward scanning, and then returns to HRS at a hold voltage (V_{hold}) of \approx 0.4 V in the backward scanning. For the negative voltages, the device demonstrates symmetric I-V curve. When the I_{CC} is set to 10^{-4} A, non-volatile bipolar RS behavior can be observed, as shown in Figure 2c. However, after several times of voltage scanning, the

-2

Voltage (V)

10-7



www.advancedsciencenews.com



www.small-journal.com

device cannot return to the HRS once it is set to the LRS, indicating the write-once read-many-times (WORM) behaviors. The positive part of the I-V curve in Figure 2c is further replotted in double logarithmic coordinates and linearly fitted (Figure \$5, Supporting Information). The slope of the fitted curve at the LRS is 0.98, indicating the Ohmic behaviors of the LRS. By considering the Cu⁺ in CIPS can migrate in the S framework and further jump out of the S octahedra when stimulated by external electric field, Cu CFs can be generated at the LRS. Once the formation of Cu CFs, the RS mechanism is dominated by the metal CFs rather than the ferroelectric polarization. Furthermore, to support our hypothesis, the *I*–*V* curves of the device at the LRS at different temperatures are measured, as shown in Figure S6 (Supporting Information). The resistance at the LRS gradually increases with the temperature, confirming the metallic conductive behaviors of the device at the LRS.^[36] Thus, it is further concluded that Cu CFs can be formed at the LRS. Moreover, the WORM RS behaviors can be attributed to the formed CFs which are stable and strong and can not be ruptured. On the other hand, the observed TS behaviors is due to the generated filaments that are limited and can not be remained at low $I_{\rm CC}$. Thus, the device returns to HRS, giving rise to the volatile TS behaviors. Such TS memristors can be utilized in artificial nociceptors, [37] basic logic gate operations, [38] and the classical LIF (Leaky Integrate-and-Fire) model.[39]

Based on the aforementioned RS mechanism, we can conclude that the device is favorable to form Cu CFs due to Cu⁺ migration in CIPS. Therefore, we investigate the RS behaviors of Cudeficient CIPS*nanosheets with a low content of Cu based on Pt/CIPS*/Pt structure. For initial devices of CIPS*, the HRS can be maintained continuously during the retention of the bias voltage of < 10 V, as shown in Figure 2d. When the applied voltage reaches up to 10 V, the device is activated and shifted to the LRS after ≈40 s, corresponding to the electroforming process of the memristor. After activation, the device exhibits typical bipolar RS behavior (Figure 2e). Figure 2f shows the retention characteristics of the device at read voltage ($\ensuremath{V_{\text{read}}}\xspace$) of 0.5 V. The LRS and HRS are distinguishable with an ON/OFF of $\approx 5 \times 10^5$ and there is no significant degradation of the HRS and LRS of the device for 10⁴ s. Subsequently, endurance performance is examined, as shown in Figure S7 (Supporting Information). Although there are some fluctuations in the HRS and LRS, the device shows good endurance performance with an ON/OFF ratio of $\sim 10^4$ during the 2150 cycles. Furthermore, the resistance states of the fabricated memristor based on CIPS* can be well tuned by the I_{CC} ranging from 1 to 100 μ A, as shown in Figure 2g. For each I_{CC} , non-volatile bipolar RS behavior can be obtained, and more importantly, we can achieve five different LRSs. Figure 2h illustrates the retention performance of the HRS and five LRSs at different I_{CC} . The resistance states can be well maintained up to 1500 s without obvious degradation and any overlaps. Moreover, we used a power-law extrapolation to extrapolate the device retention performance to 10 years, as shown in Figure S8 (Supporting Information). Such extrapolation indicates that the HRS and the 5 LRSs of the device can remain stable without any degradation or overlaps even after 10 years, demonstrating good stability of the multilevel storage.

Besides, the cycle-to-cycle variations are investigated by measuring the repeatability of an individual device. Figure S9a (Supporting Information) illustrates the I-V curves for a typical

Pt/CIPS*/Pt device repeated for 90 cycles at the I_{CC} of 10^{-5} A. Although there are some fluctuations in the SET and RESET voltages, the device consistently maintains similar conductance levels at both the LRS and HRS during the 90 cycles. In order to characterize the device-to-device variation, 40 devices based on CIPS* are successfully fabricated and the RS behaviors are measured, as shown in Figure S9b (Supporting Information). All the 40 devices demonstrate typical bipolar RS behaviors. Figure 2i shows statistical distribution of the SET and RESET voltages of the 40 devices, suggesting insignificant device-to-device variations and good reproducibility of the CIPS* based memristors. Our CIPS* devices demonstrate comparable RS behaviors with previously reported 2D ferroelectric materials, as shown in Table S1 (Supporting Information). The major difference is that we employed Cu-deficient CIPS* to achieve reliable digital RS behaviors with high endurance stability (>2000 cycles), especially compared with digital ferroelectric memristors. And, such RS can be used to realize multilevel storage, which is seldom reported in other 2D ferroelectric materials. For the RS mechanism of CIPS*, it is considered that the formation of non-stoichiometric In_{4/3}P₂S₆ (IPS) with metallic phase due to the Cu⁺ depletion in the CIPS* after Cu+ is driven by the external electric filed and then migrates to the target electrode. [24,40] Initially, the device is at the HRS where Cu⁺ is uniformly distributed in CIPS*. When a positive voltage is applied, Cu⁺ depletion in the CIPS* layer can be induced due to the migration of Cu⁺ to the Pt electrode and then reduced to Cu atoms, leading to phase transition to metallic IPS and the device transition to the LRS. When a reverse voltage is applied, the Cu atoms are oxidized to Cu⁺ and re-migrated back to the CIPS*, and the device returns to the HRS.

Furthermore, it is more interesting that the CIPS* devices show analog RS behaviors if the operation voltage is reduced. The observed analog RS behavior can be attributed to the migration of movable Cu⁺.[33] As shown in Figure 3a, the CIPS* device demonstrates typical butterfly-shape I-V hysteresis loop owing to the ferroelectric characteristics. The I-V curve in linear scale of the device is shown in the inset of Figure 3a. To study the analog RS behavior, the cyclic scanning voltages of 0 V \rightarrow + $5 \text{ V} \rightarrow 0 \text{ V}$ are applied to the device (Figure 3b). As the number of scanning increases, the current at +5 V increased from 2.01 \times 10^{-8} to 3.08×10^{-8} A. The potentiation tendency of the current is clearly shown in the inset of Figure 3b. For negative $0 \text{ V} \rightarrow -5 \text{ V} \rightarrow$ 0 V continuous scanning, the current of the device still demonstrates the potentiation tendency rather than depression trend as the number of scans increases (Figure 3c). The current at -5 V increases from -7.15×10^{-8} to -8.98×10^{-8} A, which can be clearly seen in the inset of Figure 3c. When the sweep range is reduced to 2 V, the memristor still shows butterfly-shaped I–V curve in Figure 3d and the curve in linear scale of the device is shown in the inset of Figure 3d. Interestingly, the device exhibits depression trends when the voltage amplitude is reduced to 2 V, as shown in Figure 3e.f. Thus, the CIPS* device is capable of implementing potentiation and depression behaviors. However, the potentiation and depression are dependent on the voltage amplitude rather than the voltage polarity, which is different from the majority of memristors that with the potentiation and depression relying on the voltage polarity.

Based on aforementioned studies for the RS performance of CIPS and CIPS*, we can conclude that the Pt/CIPS/Pt

16136829, 0. Downloaded from https://onlinelibrary.wiely.com/doi/10.1002/smll.202412314 by HONG KONG POLYTECHINC UNIVERSITY HUNG HOM, Viley Online Library on [05/10/2025]. See the Terms and Conditions (https://onlinelibrary.wiely.com/terms

-and-conditions) on Wiley Online Library for rules of use; OA articles are governed by the applicable Creative Commons License

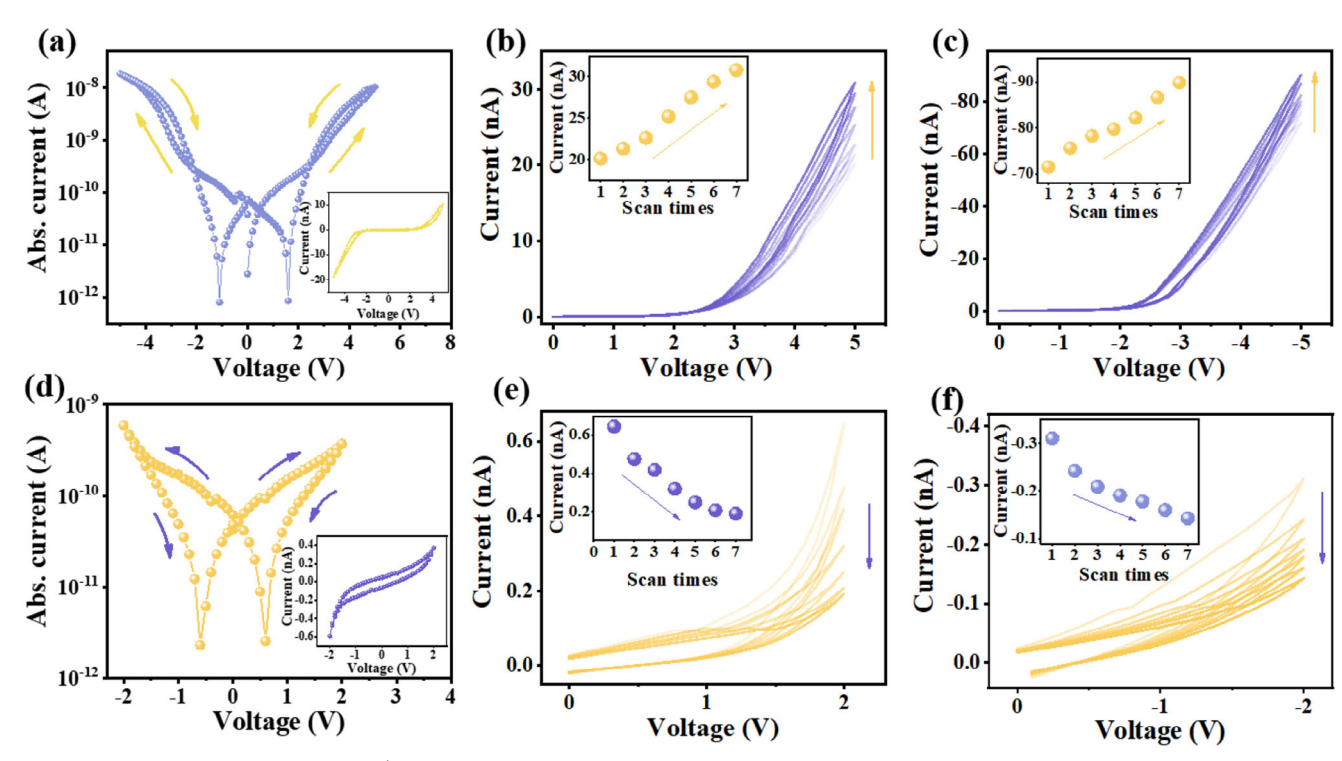


Figure 3. Analog RS behavior of the CIPS* memristors. a) Typical analog RS behavior at the operation voltage of 5 V. The I-V curve with linear scale is shown in the inset. b) Seven cycles of I-V curves for positive voltage sweeping 0 V \rightarrow + 5 V \rightarrow 0 V. The inset shows the current values recorded at 5 V. c) Seven cycles of I-V curves for negative voltage sweeping 0 V \rightarrow - 5 V \rightarrow 0 V. The inset shows the current values recorded at - 5 V. d) Typical analog RS behavior at the operation voltage of 2 V. The I-V curve with linear scale is shown in the inset. e) Seven cycles of I-V curves for positive voltage sweeping 0 V \rightarrow + 2 V \rightarrow 0 V. The inset shows the current values recorded at 2 V. f) Seven cycles of I-V curves for negative voltage sweeping 0 V \rightarrow - 2 V \rightarrow 0 V. The inset shows the current values recorded at - 2 V.

memristors demonstrate volatile TS and non-volatile WORM behaviors by tuning the I_{CC} . On the other hand, Pt/CIPS*/Pt memristors show non-volatile bipolar RS and analog RS behaviors by controlling the operation voltage. And more importantly, Pt/CIPS*/Pt memristors exhibit high endurance stability (>2000 cycles). While, for Pt/CIPS/Pt, after several times of voltage scanning, the device demonstrates WORM behaviors. Furthermore, Pt/CIPS*/Pt memristors can achieve multilevel storage, which is not observed in our Pt/CIPS/Pt devices. Moreover, Pt/CIPS*/Pt memristors not only demonstrate digital RS behaviors with good endurance characteristics and retention performance, but also achieve analog RS behaviors, which is beneficial to synaptic applications and neuromorphic computing.

Two-terminal devices with analog RS can be utilized to emulate biological synapse which is a key part of the information transmission between two neurons. [41] As shown in **Figure 4a**, the synapse consists of three parts, the presynaptic membrane, the synaptic gap and the postsynaptic membrane. [42] The two terminal memristors can be used for implementing synaptic functions when stimulated by the pulse voltages. When 20 consecutive pulses with amplitude of 4 V are applied to the device, the conductance of the device increases gradually regardless of the polarity of the pulses. On the other hand, when the amplitude of the pulses is reduced to 2 V, the conductance of the device decreases successively regardless of the polarity of the pulses. This means that the device has polarity-independent and amplitude-dependent LTP and LTD behaviors with good conductance mod-

ulation. In our experiments, we can achieve the LTP/LTD series by applying +4 V/ +2 V, +4 V/ -2 V, -4 V/ +2 V, or -4 V/ -2 Vpulse series, as respectively shown in Figure 4b,e. Figure S10 (Supporting Information) shows the LTP behaviors for the pulse amplitude increased from 4 to 5 V (as well as from -4 to -5 V) with different pulse durations (W) and pulse intervals (Δt). Figure S11 (Supporting Information) shows the LTD behaviors for the pulse amplitude increased from 1 to 2 V (as well as from -1 to -2 V) with different W and Δt . For relatively high voltage pulses, the device demonstrates LTP functions. And, the potentiation effects can be further enhanced with the increase in pulse amplitude and pulse duration, as well as the decrease in pulse interval, regardless of the positive or negative pulse voltages. For relatively low voltage pulses, the device demonstrates LTD functions with similar tendency. All these measurements indicate that the polarity-independent and amplitude-dependent LTP and LTD behaviors can be achieved based on our CIPS* synaptic memristors. Furthermore, it is essential to understand the observed unusual RS behaviors and synaptic functions for CIPS*. The underlying mechanism of the unusual RS behaviors can be understood by the competition between the ferroelectric polarization and ionic conductivity in CIPS*. At a relatively high voltage (5 V), Cu⁺ ions start to migrate out of the lattice. However, in the case of analog RS, most of the RS layer is CIPS* rather than metallic IPS. The interlayer Cu⁺ ions can contribute to the ionic conductivity in CIPS*, leading to an increase in the conductance of the device as the sweeping number. At relatively low voltages (2 V),

16136829, 0, Downloaded from https://onlinelibrary.wiley.com/doi/10.1002/smll.202412314 by HONG KONG POLYTECHNIC UNIVERSITY HU NG HOM, Wiley Online Library on [05/10/2025]. See the Terms and Conditions (https://online

nelibrary.wiley.com/terms-and-conditions) on Wiley Online Library for rules of use; OA articles are governed by the applicable Creative Commons

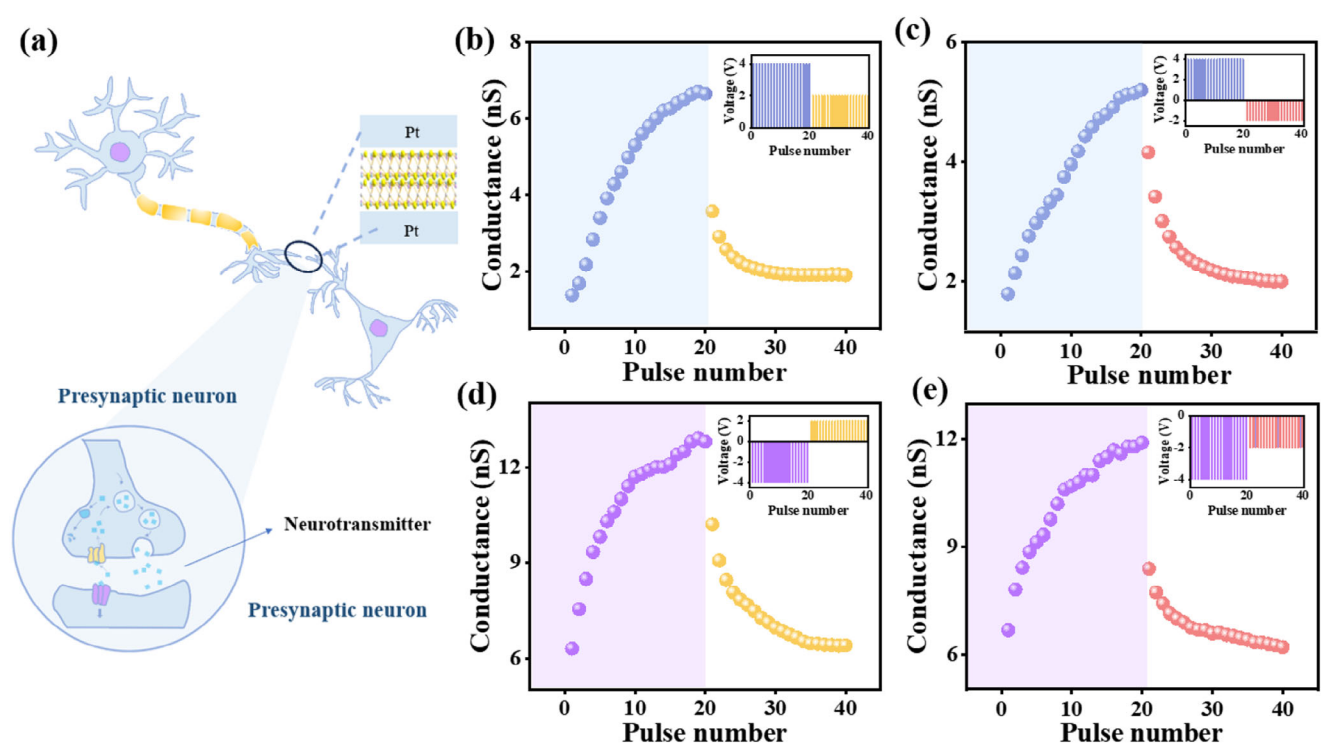


Figure 4. Synaptic functions based on the CIPS* memristors. a) Schematic of the structure of neurons, biological synapses, and devices. LTP and LTD behaviors stimulated by 20 consecutive pulses with amplitude of +4 and +2 V, b), of +4 and -2 V, c), of -4 and +2 V, d) and of -4 and -2 V, e).

Cu⁺ can only migrate in the lattice, giving rise to the non-volatile ferroelectric polarization. In this case, the cyclic scanning of the voltage continuously contributes to the ferroelectric polarization rather than the ionic conductivity in the CIPS*. Besides, it is found the conductance value decrease sharply when the pulse amplitude is changed from 4 to 2 V, or from -4 to -2 V in the LTP/LTD functions. It is the ionic conductivity arising from the interlayer Cu⁺ ions that dominates the LTP behaviors, while, it is the ferroelectric polarization that determines the LTD functions. When the stimulated pulses are changed from high to low amplitude, the ionic conductivity is dramatically decreased, inducing the sharp decrease in the conductance value. Currently, it is relatively convenient to detect the Cu⁺ ions migration for CIPS in planer memristors. [25,33,43] However, it is relatively difficult to successfully prepare the cross-section samples for direct observation of Cu⁺ ions migration in vertical memristors due to the random locations of the Cu⁺ ions in the intralayer and interlayer. Some cross-section accurate positioning techniques or pre-designed positioning markers during device preparation may be suitable for the direct Cu⁺ ion migration observation in vertical devices. Furthermore, automatic identification algorithms based on machine vision could be developed to achieve intelligent identification in such randomly distributed devices. Therefore, to further verify the migration behaviors of Cu⁺ ions in our CIPS*nanosheets, Raman spectroscopy has been used to detect the different states of the devices.[23,24,30,33] As shown in Figure S12 (Supporting Information), the Raman spectra of CIPS* are obtained in different states (initial, 2 V and 5 V). When a relatively high voltage of 5 V is applied, the intensity of the Raman peak at 317 cm⁻¹ decreases and even vanishes, which is attributed to the redistribution of Cu⁺ ions out of the S octahedral voids.^[30] And the increase in Raman peak intensity at the 254 cm⁻¹ indicates the lattice deformation after Cu⁺ ions migration.^[23] When a relatively low voltage of 2 V is applied, the Raman peaks is almost same to the initial state, suggesting the Cu⁺ ions are still in the S octahedral voids. These Raman results can confirm the longdistance migration of the Cu⁺ ions in our Cu-deficient CIPS* nanosheets.

Moreover, the short-term plasticity of paired-pulse facilitation (PPF) is examined, as shown in Figure 5a. The PPF index can be achieved according to the calculation of $(A_2 - A_1)/A_1 \times 100\%$, where A₁ and A₂ are the peak values of the recorded currents of the first and second pulse when two successive pulses are applied, respectively.[44] The fitting data indicate that the PPF index is decreased exponentially with the pulse interval, which is consistent with the PPF effect in biological synapses. Furthermore, continuous LTP/LTD series can be achieved by applying pulse series of 20 consecutive pulses of +4 V (W = 200 ms, $\Delta t = 100 \text{ ms}$) and 20 consecutive pulses of -2 V (W = 200 ms, $\Delta t = 100$ ms). Figure 5b shows 6 cycles of LTP and LTD with good reproducibility. The experimentally obtained LTP/LTD cycles are used for recognition of handwritten digit.[45] As shown in Figure 5c,a three-layer ANN is composed of input, hidden and output layers. Figure 5d is the array diagram of matrix operation. The recognition accuracy of handwritten digital images from the National Institute of Standards and Technology (MNIST) handwriting dataset is examined. After 40 training epochs, the recognition accuracy for a small handwritten digital image of 8 x 8 pixels can reach up to 91.15%, as shown in Figure 5e. Furthermore, in order to evaluate the effects of the cycle-to-cycle and

161 36829, 0, Downloaded from https://onlinelibrary.wiley.com/doi/10.1002/smll.202412314 by HONG KONG POLYTECHNIC UNIVERSITY HUNG HOM, Wiley Online Library on [05/10/2025]. See the Terms and Conditions (https://onlinelibrary.wiley.com/doi/10.1002/smll.202412314 by HONG KONG POLYTECHNIC UNIVERSITY HUNG HOM, Wiley Online Library on [05/10/2025]. See the Terms and Conditions (https://onlinelibrary.wiley.com/doi/10.1002/smll.202412314 by HONG KONG POLYTECHNIC UNIVERSITY HUNG HOM, Wiley Online Library on [05/10/2025]. See the Terms and Conditions (https://onlinelibrary.wiley.com/doi/10.1002/smll.202412314 by HONG KONG POLYTECHNIC UNIVERSITY HUNG HOM, Wiley Online Library on [05/10/2025]. See the Terms and Conditions (https://onlinelibrary.wiley.com/doi/10.1002/smll.202412314 by HONG KONG POLYTECHNIC UNIVERSITY HUNG HOM, Wiley Online Library on [05/10/2025]. See the Terms and Conditions (https://onlinelibrary.wiley.com/doi/10.1002/smll.202412314 by HONG KONG POLYTECHNIC UNIVERSITY HUNG HOM, Wiley Online Library on [05/10/2025]. See the Terms and Conditions (https://onlinelibrary.wiley.com/doi/10/2025).

and-conditions) on Wiley Online Library for rules of use; OA articles are governed by the applicable Creative Commons

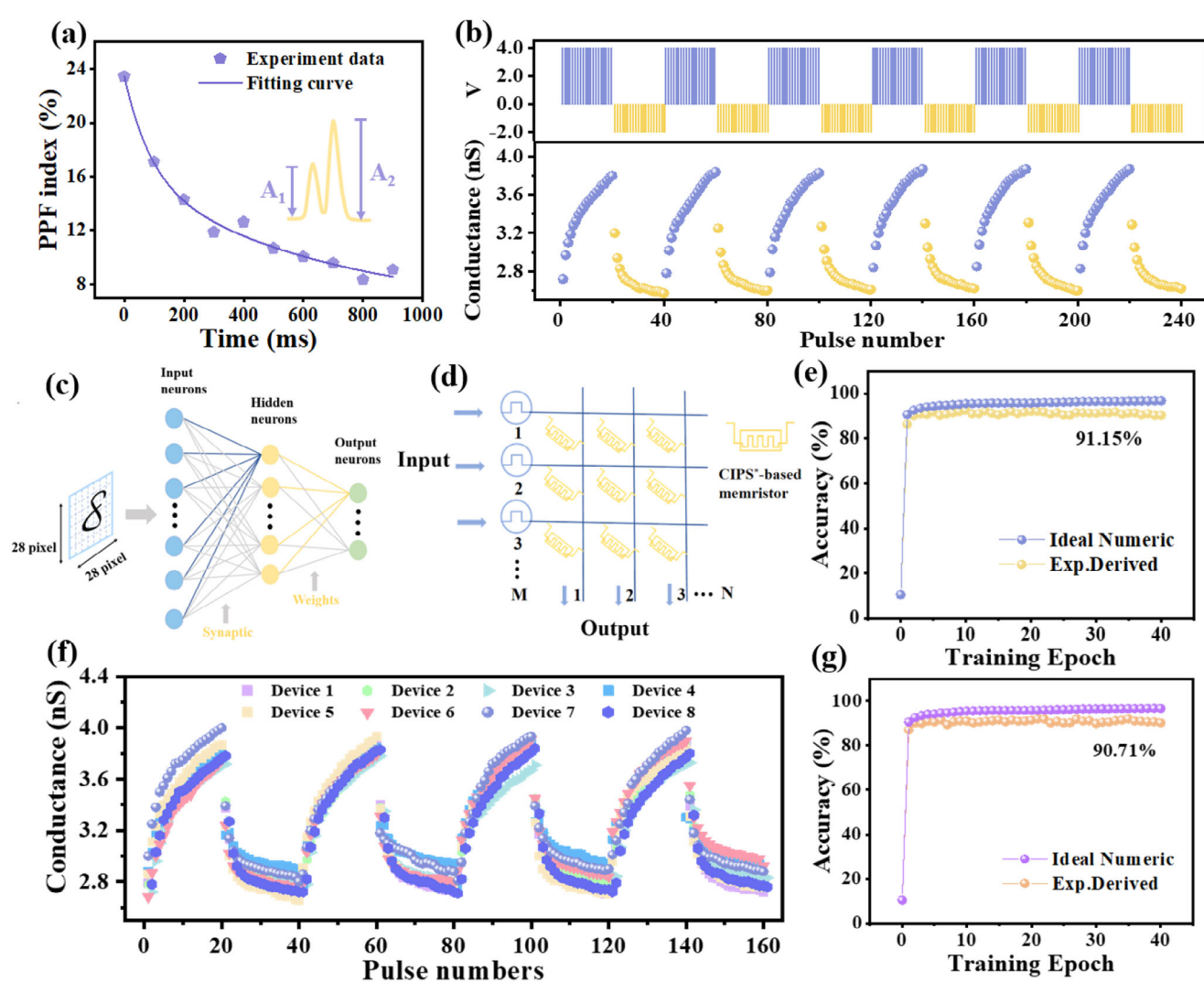


Figure 5. a) PPF index as a function of the interval of the two consecutive pulse pairs. b) Six sets of repeatable LTP/LTD behaviors stimulated by 20 consecutive pulses with amplitude of +4 and -2 V. c) Schematic of a three-layer artificial neural network for image recognition. d) Schematic of the crossbar array used for matrix operations. e) Recognition accuracy of the artificial neural network as a function of the training epoch. f) The LTP/LTD behaviors for the 8 synaptic memristors, for each device 4 cycles of LTP and LTD are demonstrated. g) The recognition accuracy after considering the cycle-to-cycle and device-to-device variations on the neural network simulation.

device-to-device variations on the training results, we incorporated these variabilities of 8 devices to perform a handwritten digit recognition simulation. [46] Figure 5f shows the conductance variations of 8 different synaptic memristors, for each device 4 cycles of LTP and LTD are demonstrated. As shown in Figure 5g, although the accuracy is lower than that for the ANN without considering these variations, the accuracy remains as high as 90.71% even after considering the such variations of the synaptic functions on the neural network simulation.

3. Conclusion

In summary, Cu-deficient CIPS* nanosheets are prepared and the RS behaviors and synaptic functions are systematically investigated. Different from CIPS with controllable TS and WORM behaviors, CIPS* memristors show non-volatile bipolar RS and ana-

log RS behaviors by controlling the operation voltage. And more importantly, Pt/CIPS*/Pt memristors exhibit high endurance stability (>2000 cycles). While, for Pt/CIPS/Pt, after several times of voltage scanning, the device demonstrates WORM behaviors. Furthermore, Pt/CIPS*/Pt memristors can achieve multilevel storage, which is not observed in our Pt/CIPS/Pt devices. Moreover, Pt/CIPS*/Pt memristors not only demonstrate digital RS behaviors with good endurance characteristics and retention performance, but also exhibit analog RS behaviors. And more intriguing, amplitude-dependent and polarity-independent LTP and LTD can be simulated based on the analog memristors. The recognition accuracy of handwritten digital images can reach up to 91.15%. Even after considering the cycle-to-cycle and device-todevice variations of the synaptic functions, the accuracy remains as high as 90.71%, demonstrating the great potential of the CIPS* for applications in neuromorphic computing.

and-conditions) on Wiley Online Library for rules of use; OA articles are governed by the applicable Creative Commons

www.advancedsciencenews.com



4. Experimental Section

Material Preparation and Device Fabrication: 2D CIPS and CIPS* nanosheets were prepared by the typical mechanical exfoliation method and then transferred onto the SiO₂ (280 nm)/Si substrates for characterizations and device fabrication. In this experiments, 2D CIPS and CIPS* nanosheets were exfoliated by using Scotch tape from their bulk materials which were commercially purchased. Then, the exfoliated nanosheets were transferred onto a 280-nm SiO₂ coated Si substrate. For the two-terminal memristors with sandwiched structure of Pt/CIPS/Pt, bottom electrode of Pt was first prepared by a standard photolithography technique and sputtering method, then the exfoliated CIPS and CIPS* nanosheets were transferred directly onto the Pt bottom electrode with the help of polymethyl methacrylate (PMMA). After that, the Pt top electrode was prepared onto the top surface of the transferred nanosheet without contact to the bottom Pt electrode.

Characterizations, Measurements and Simulations: XRD (Rigaku/MiniFlex) was used to characterize the crystal structure of CIPS and CIPS* materials. Raman spectrometer (HORIBA LabRAM HR Evolution) with the laser wavelength of 532 nm was employed to study the exfoliated CIPS and CIPS* nanosheets. XPS (Thermo Scientific/ESCALAB 250 Xi) was used for elemental analysis of the CIPS and CIPS* nanosheets. SEM (Zeiss/Sigma 500, UK) was utilized to characterize the surface morphology and EDS was employed to examine element distribution of the exfoliated CIPS and CIPS* nanosheets. AFM (Park Systems Crop XE7) was adopted to determine the thickness of the CIPS and CIPS* nanosheets. All electrical properties were tested by using a four-probe station system equipped with a source meter (Keithley 2636B) at room temperature in air. For neuromorphic computing simulations, the program code was written in Python according to the back propagation algorithm and with the help of neural core provided by the CrossSim platform. In this experiments, repeatable LTP/LTD cycles were first needed. Then, the repeatability of each conductance state in the weight updating process was counted through the code, and completed the weight upgrade of the neural network with this probability. In the CrossSim platform, this type of weight update was called Look up table model. The program was run under Spyder, a free integrated development environment.

Supporting Information

Supporting Information is available from the Wiley Online Library or from the author.

Acknowledgements

This work was supported by the grants from National Natural Science Foundation of China (No. 62474118, 52233014 and 62411560160), RGC grant (PolyU SRFS2122-5S02) and PolyU grants (1-CD7V and 1-CE0H).

Conflict of Interest

The authors declare no conflict of interest.

Data Availability Statement

The data that support the findings of this study are available from the corresponding author upon reasonable request.

Keywords

CIPS, Cu deficiency, ferroelectric, memristors, neuromorphic computing

Received: December 17, 2024 Revised: May 8, 2025 Published online:

- [1] S. Li, F. Wang, Y. Wang, J. Yang, X. Wang, X. Zhan, J. He, Z. Wang, Adv. Mater. 2024, 36, 2301472.
- [2] S. Lin, G. Zhang, Q. Lai, J. Fu, W. Zhu, H. Zeng, Adv. Funct. Mater. 2023, 33, 2304139.
- [3] F. Guo, M. Song, M.-C. Wong, R. Ding, W. F. Io, S.-Y. Pang, W. Jie, J. Hao, Adv. Funct. Mater. 2022, 32, 2108014.
- [4] Y. Huang, J. L. Gottfried, A. Sarkar, G. Zhang, H. Lin, S. Ren, Nat. Commun. 2023, 14, 5041.
- [5] S. Zhou, L. You, A. Chaturvedi, S. A. Morris, J. S. Herrin, N. Zhang, A. Abdelsamie, Y. Hu, J. Chen, Y. Zhou, S. Dong, J. Wang, *Mater. Horiz.* 2020, 7, 263.
- [6] M. A. Susner, M. Chyasnavichyus, M. A. Mcguire, P. Ganesh, P. Maksymovych, Adv. Mater. 2017, 29, 1602852.
- [7] F. Liu, L. You, K. L. Seyler, X. Li, P. Yu, J. Lin, X. Wang, J. Zhou, H. Wang, H. He, S. T. Pantelides, W. Zhou, P. Sharma, X. Xu, P. M. Ajayan, J. Wang, Z. Liu, Nat. Commun. 2016, 7, 12357.
- [8] S. Zhou, L. You, H. Zhou, Y. Pu, Z. Gui, J. Wang, Front. Phys. 2020, 16, 13301.
- [9] R. He, H. Wang, F. Liu, S. Liu, H. Liu, Z. Zhong, Phys. Rev. B. 2023, 108. 024305.
- [10] P. Singh, S. Baek, H. H. Yoo, J. Niu, J.-H. Park, S. Lee, ACS Nano 2022, 16, 5418.
- [11] J. Niu, S. Jeon, D. Kim, S. Baek, H. H. Yoo, J. Li, J.-S. Park, Y. Lee, S. Lee, *InfoMat.* 2024, 6, 12490.
- [12] Q. Wang, T. Xie, N. A. Blumenschein, Z. Song, J. C. Kotsakidis, A. T. Hanbicki, M. A. Susner, B. S. Conner, Q. Tan, S. H. Lee, Z. Mao, X. Ling, T. Low, J.-P. Wang, A. L. Friedman, C. Gong, *Matter* 2022, 5, 4425
- [13] J. Zhou, A. Chen, Y. Zhang, D. Pu, B. Qiao, J. Hu, H. Li, S. Zhong, R. Zhao, F. Xue, Y. Xu, K. P. Loh, H. Wang, B. Yu, Adv. Mater. 2023, 35, 2302419
- [14] Y. Zhang, J. Mao, R.-K. Zheng, J. Zhang, Y. Wu, X. Wang, K. Miao, H. Yao, L. Yang, H. Zheng, Adv. Funct. Mater. 2023, 33, 2214745.
- [15] D. Zhang, Z.-D. Luo, Y. Yao, P. Schoenherr, C. Sha, Y. Pan, P. Sharma, M. Alexe, J. Seidel, *Nano Lett.* **2021**, *21*, 995.
- [16] N. Balke, S. M. Neumayer, J. A. Brehm, M. A. Susner, B. J. Rodriguez, S. Jesse, S. V. Kalinin, S. T. Pantelides, M. A. Mcguire, P. Maksymovych, ACS Appl. Mater. Interfaces. 2018, 10, 27188.
- [17] C. Kaspar, B. J. Ravoo, W. G. Van Der Wiel, S. V. Wegner, W. H. P. Pernice, *Nature* 2021, 594, 345.
- [18] J. He, R. Wei, S. Ge, W. Wu, J. Guo, J. Tao, R. Wang, C. Wang, C. Pan, InfoMat 2024, 6, 12493.
- [19] X. Duan, Z. Cao, K. Gao, W. Yan, S. Sun, G. Zhou, Z. Wu, F. Ren, B. Sun, Adv. Mater. 2024, 36, 2310704.
- [20] Z. Cao, B. Sun, G. Zhou, S. Mao, S. Zhu, J. Zhang, C. Ke, Y. Zhao, J. Shao, *Nanoscale Horiz.* 2023, 8, 716.
- [21] C. Teng, Q. Yu, Y. Sun, B. Ding, W. Chen, Z. Zhang, B. Liu, H.-M. Cheng, *InfoMat.* 2023, 5, 12351.
- [22] B. Zhao, X. Zhao, Q. Li, X. Xun, T. Ouyang, Z. Zhang, Z. Kang, Q. Liao, Y. Zhang, *InfoMat* 2022, 4, 12350.
- [23] W. Ci, P. Wang, W. Xue, H. Yuan, X. Xu, Adv. Funct. Mater. 2024, 34, 2316360.
- [24] Z. Zhong, S. Wu, X. Li, Z. Wang, Q. Yang, B. Huang, Y. Chen, X. Wang, T. Lin, H. Shen, X. Meng, M. Wang, W. Shi, J. Wang, J. Chu, H. Huang, ACS Nano 2023, 17, 12563.
- [25] Y. Sun, R. Zhang, C. Teng, J. Tan, Z. Zhang, S. Li, J. Wang, S. Zhao, W. Chen, B. Liu, H.-M. Cheng, *Mater. Today.* 2023, 66, 9.
- [26] Y. Wu, N. T. Duong, Y.-C. Chien, S. Liu, K.-W. Ang, Adv. Electron. Mater. 2024, 10, 2300481.
- [27] Y. Liu, Y. Wu, H. Han, Y. Wang, R. Peng, K. Liu, D. Yi, C.-W. Nan, J. Ma, Adv. Funct. Mater. 2024, 34, 2306945.
- [28] B. Li, S. Li, H. Wang, L. Chen, L. Liu, X. Feng, Y. Li, J. Chen, X. Gong, K.-W. Ang, Adv. Electron. Mater. 2020, 6, 2000760.



www.advancedsciencenews.com



- [29] X. Jiang, X. Wang, X. Wang, X. Zhang, R. Niu, J. Deng, S. Xu, Y. Lun, Y. Liu, T. Xia, J. Lu, J. Hong, *Nat. Commun.* 2022, 13, 574.
- [30] H. Zhu, J. Li, Q. Chen, W. Tang, X. Fan, F. Li, L. Li, ACS Nano 2023, 17, 1239.
- [31] R. Rao, R. Selhorst, J. Jiang, B. S. Conner, R. Siebenaller, E. Rowe, A. N. Giordano, R. Pachter, M. A. Susner, *Chem. Mater.* 2023, 35, 8020.
- [32] R. Rao, R. Selhorst, B. S. Conner, M. A. Susner, Phys. Rev. Mater. 2022, 6, 045001.
- [33] J. Chen, C. Zhu, G. Cao, H. Liu, R. Bian, J. Wang, C. Li, J. Chen, Q. Fu, Q. Liu, P. Meng, W. Li, F. Liu, Z. Liu, Adv. Mater. 2022, 34, 2104676.
- [34] Z. Feng, S. Wang, Z. Zhou, Y. Hu, Q. Li, J. Xue, Q. Yan, Z. Luo, R. Feng, Y. Weng, L. Fang, L. You, Appl. Phys. Lett. 2024, 124, 012903.
- [35] B. Lin, A. Chaturvedi, J. Di, L. You, C. Lai, R. Duan, J. Zhou, B. Xu, Z. Chen, P. Song, J. Peng, B. Ma, H. Liu, P. Meng, G. Yang, H. Zhang, Z. Liu, F. Liu, Nano Energy 2020, 76, 104972.
- [36] P. Lei, H. Duan, L. Qin, X. Wei, R. Tao, Z. Wang, F. Guo, M. Song, W. Jie, J. Hao, Adv. Funct. Mater. 2022, 32, 2201276.

- [37] J. H. Yoon, Z. Wang, K. M. Kim, H. Wu, V. Ravichandran, Q. Xia, C. S. Hwang, J. J. Yang, *Nat. Commun.* 2018, 9, 417.
- [38] L. Zhong, W. Xie, J. Yin, W. Jie, J. Mater. Chem. C. 2023, 11, 5032.
- [39] B. Xie, X. Zhang, S. Cheng, W. Jie, Mater. Des. 2022, 222, 111090.
- [40] S. M. Neumayer, M. Si, J. Li, P.-Y. Liao, L. Tao, A. O'hara, S. T. Pantelides, P. D. Ye, P. Maksymovych, N. Balke, ACS Appl. Mater. Interfaces 2022, 14, 3018.
- [41] R. Yang, H.-M. Huang, X. Guo, Adv. Electron. Mater. 2019, 5, 1900287.
- [42] Z. Peng, Z. Cheng, S. Ke, Y. Xiao, Z. Ye, Z. Wang, T. Shi, C. Ye, X. Wen, P. K. Chu, X.-F. Yu, J. Wang, Adv. Funct. Mater. 2023, 33, 2211269.
- [43] Z. Zhong, X. Cheng, W. Song, Q. Yang, X. Li, Y. Wang, W. Wang, Y. Zhuang, Y. Chen, W. Shi, Device. 2025.
- [44] Z. Dang, F. Guo, Y. Zhao, K. Jin, W. Jie, J. Hao, Adv. Funct. Mater. 2024, 34, 2400105.
- [45] Z. Dang, F. Guo, Z. Wang, W. Jie, K. Jin, Y. Chai, J. Hao, ACS Nano 2024, 18, 27727.
- [46] S.-T. Yang, X.-Y. Li, T.-L. Yu, J. Wang, H. Fang, F. Nie, B. He, L. Zhao, W.-M. Lü, S.-S. Yan, A. Nogaret, G. Liu, L.-M. Zheng, Adv. Funct. Mater. 2022. 32, 2202366.